Effects of Uniaxial Distortion on the Stability of Square Skyrmion Crystals in Noncentrosymmetric Magnets

Satoru Hayami *

Posted Date: 2 February 2026

doi: 10.20944/preprints202602.0033.v1

Keywords: skyrmion crystal; Dzyaloshinskii-Moriya interaction; uniaxial distortion; square lattice; multiple-Q states; scalar spin chirality

 doi:10.20944/preprints202602.0033.v1

Article

Effects of Uniaxial Distortion on the Stability of Square Skyrmion Crystals in Noncentrosymmetric Magnets

Satoru Hayami

Graduate School of Science, Hokkaido University, Sapporo 060-0810, Japan; hayami@phys.sci.hokudai.ac.jp

Abstract

We theoretically investigate the influence of uniaxial distortion on the stability of square skyrmion crystals, which are described as double-Q spin textures composed of two orthogonal spiral modulations, in noncentrosymmetric magnets. An effective spin model incorporating momentum-resolved frustrated exchange interactions and Dzyaloshinskii-Moriya (DM) interactions is analyzed using simulated-annealing calculations at low temperatures. The results reveal that uniaxial distortion drives a transformation from the double-Q square skyrmion crystal to a single-Q tilted conical spiral or vertical spiral state. The low-temperature phase diagrams further show that the stability region of the skyrmion crystal expands with increasing the magnitude of the DM interaction, making the phase more robust against the uniaxial anisotropy between exchange interactions parallel and perpendicular to the distortion axis. This study provides insight into how uniaxial strain and DM interactions cooperatively influence the formation and stability of skyrmion crystal phases in noncentrosymmetric magnetic systems.

Keywords: skyrmion crystal; Dzyaloshinskii-Moriya interaction; uniaxial distortion; square lattice; multiple-Q states; scalar spin chirality

1. Introduction

Magnetic skyrmions are topologically protected spin textures characterized by a quantized topological number, which endows them with robustness against perturbations and gives rise to a variety of emergent electromagnetic phenomena. Since their theoretical conception by Skyrme [1,2], skyrmion structures have been studied in diverse physical systems, such as liquid crystals [3–7], quantum Hall magnets [8–14], Bose-Einstein condensates [15–20], and ferroelectrics [21–25]. In magnetic materials, skyrmions appear as nanoscale swirling arrangements of localized spins [26,27], and their periodic arrangement, the skyrmion crystal (SkX), was first discovered in noncentrosymmetric chiral magnets such as MnSi [28–30], $Fe_{1-x}Co_xSi$ [31,32], FeGe [33,34], and Cu_2OSeO_3[35–37]. These discoveries sparked enormous research interest, motivated by both the fundamental topological nature of skyrmions and their promise for spintronic applications such as racetrack memory and neuromorphic computing [38–44].

In noncentrosymmetric chiral magnets, the Dzyaloshinskii-Moriya (DM) interaction [45,46] plays a decisive role in stabilizing a single-Q spiral state and SkXs [47–50]. These SkXs provide an ideal platform to explore a wide range of emergent phenomena, including the topological Hall effect [30,51–56], collective excitations [57–62], and field- or temperature-induced phase transitions [63–66]. Meanwhile, extensive theoretical efforts have demonstrated that similar topological spin textures can also emerge in centrosymmetric magnets, where SkXs arise from competing exchange interactions [67–71], magnetic anisotropies [72–79], dipolar interactions [80,81], and sublattice-dependent staggered DM interactions [82,83]. These findings have expanded the scope of materials hosting SkXs beyond conventional chiral systems.

 doi:10.20944/preprints202602.0033.v1

One of the intriguing research directions has been paid to square-lattice magnets, since such a system provides a simpler situation compared to triangular-lattice magnets owing to the absence of geometrically frustrated structures. There, multiple symmetry-related ordering wave vectors naturally allow for double-Q spin textures, such as square SkXs. Such SkXs characterized by the double-Q spin configuration have been observed in both noncentrosymmetric and centrosymmetric systems, including Co-Zn-Mn alloys [84–88], Cu_2OSeO_3[89,90], $GdRu_2Si_2$ [91–95], and $EuNiGe_3$ [96]. Theoretically, their stability has been attributed to the interplay between multiple interactions and magnetic anisotropies, which collectively govern the relative phases of helical modulations. The typical mechanisms include the DM interaction [63], momentum-space frustration [97,98], bond-dependent interaction [99,100], dipolar interaction [80], and multi-orbital effects [101]. Understanding how these microscopic ingredients stabilize or destabilize the square SkX is thus a central question in the study of topological spin textures [102].

Among various external perturbations, uniaxial distortion, which originates from epitaxial strain and applied pressure, has emerged as a key factor that can significantly modify the stability of SkXs [103–107]. By lowering the lattice symmetry and breaking the equivalence of orthogonal ordering wave vectors, distortion introduces a natural anisotropy in the competing double-Q spin configurations [108]. Experimentally, such effects have been reported in the centrosymmetric tetragonal compound $EuAl_4$, where multiple SkX phases occur under rhombic distortion [109–113]. However, a comprehensive theoretical understanding of how uniaxial distortion affects the stability of square SkXs, especially in noncentrosymmetric systems with the DM interaction, remains limited.

In this study, we investigate the stability and evolution of square SkXs under uniaxial distortion in noncentrosymmetric tetragonal magnets. We employ an effective spin model on a two-dimensional square lattice that includes momentum-resolved frustrated exchange interactions and DM interaction. Using simulated annealing, we construct low-temperature magnetic phase diagrams and clarify how uniaxial anisotropy drives topological phase transitions among the double-Q SkX, single-Q tilted conical spiral state, and the single-Q vertical spiral state. We also demonstrate that stronger DM interaction enhances the robustness of the SkX against distortion by widening its stability region in the phase diagram. The results provide microscopic insight into the cooperative role of uniaxial strain and DM interactions in realizing topological spin textures.

The remainder of this paper is organized as follows. Section 2 introduces the model Hamiltonian and numerical methods. Section 3 presents the calculated magnetic phase diagrams, magnetic-field and uniaxial distortion dependence of order parameters, and real-space spin structures in several representative model parameters. Section 4 summarizes the main findings and discusses their implications for strain-engineered control of SkXs in noncentrosymmetric magnets.

2. Model and Method

We study a classical spin system on a two-dimensional square lattice that possesses fourfold rotational symmetry but lacks spatial inversion symmetry, corresponding to the polar point group C_{4v}. The lattice constant is set to unity throughout this work. The magnetic interactions are formulated in momentum space so that the dominant instabilities at specific wave vectors can be treated explicitly. The effective spin Hamiltonian is written as

$$\mathcal{H} = -2\sum_{\nu}\left[J_{\boldsymbol{Q}_\nu}\boldsymbol{S}_{\boldsymbol{Q}_\nu}\cdot\boldsymbol{S}_{-\boldsymbol{Q}_\nu} + i\boldsymbol{D}_{\boldsymbol{Q}_\nu}\cdot(\boldsymbol{S}_{\boldsymbol{Q}_\nu}\times\boldsymbol{S}_{-\boldsymbol{Q}_\nu})\right] - \sum_i \boldsymbol{H}\cdot\boldsymbol{S}_i, \tag{1}$$

where $\boldsymbol{S}_{\boldsymbol{Q}_\nu} = (S^x_{\boldsymbol{Q}_\nu}, S^y_{\boldsymbol{Q}_\nu}, S^z_{\boldsymbol{Q}_\nu})$ is the Fourier component of the classical spin $\boldsymbol{S}_i = (S^x_i, S^y_i, S^z_i)$ with fixed length $|\boldsymbol{S}_i| = 1$. The summation runs over two symmetry-related ordering wave vectors, $\boldsymbol{Q}_1 = (\pi/4, 0)$ and $\boldsymbol{Q}_2 = (0, \pi/4)$, by the fourfold rotational operation. The prefactor of two in Eq. (1) accounts for the equivalent contributions from $\pm\boldsymbol{Q}_\nu$.

The first term describes the momentum-resolved isotropic exchange interaction, characterized by the coupling constants $J_{\boldsymbol{Q}_\nu}$. In the tetragonal structure, the fourfold rotational symmetry ensures $J_{\boldsymbol{Q}_1} =$

 doi:10.20944/preprints202602.0033.v1

J_{Q_2}. To capture anisotropic effects, we define the ratio $\gamma_{Q_2} = J_{Q_2}/J_{Q_1}$ and set $J_{Q_1} = 1$ as the energy unit. The form of this interaction originates from frustrated short-range exchange interactions [114–118] or long-range Ruderman-Kittel-Kasuya-Yosida-type interactions [119–121] arising from Fermi-surface nesting [122–124], both of which can produce multiple wave-vector instabilities in momentum space. We restrict the model to the $\boldsymbol{Q}_1$ and $\boldsymbol{Q}_2$ channels, assuming that these wave vectors dominate the magnetic instability, while higher harmonics are neglected for simplicity. Such a simplification allows an efficient exploration of the emergence and stability of multiple-Q states, offering microscopic insight into experimentally observed behaviors in materials such as $Y_3Co_8Sn_4$ [125], $EuNiGe_3$ [96], and EuPtSi [126].

The second term in Eq. (1) represents the antisymmetric DM interaction allowed by the lack of spatial inversion symmetry. For the C_{4v} symmetry, the DM vectors satisfy $D^y_{Q_1} = -D^x_{Q_2} \equiv D$, and all other components vanish. This term introduces a fixed helicity to the spin modulation, favoring a spiral structure determined by the sign of D. Other anisotropic terms that are symmetry-allowed but secondary in strength for small spin–orbit coupling, such as bond-dependent symmetric exchange interaction [127–133], are omitted here for clarity [134]. The final term denotes the Zeeman coupling to an external magnetic field $\boldsymbol{H} = (0, 0, H)$ applied along the out-of-plane direction.

To investigate the effect of symmetry lowering, we introduce a uniaxial distortion along the [100] direction. This perturbation reduces the crystal symmetry from tetragonal to orthorhombic and removes the equivalence between the two ordering wave vectors. In our model, this distortion is incorporated solely through the anisotropy of the coupling constants, so that $J_{Q_1} \neq J_{Q_2}$ (or equivalently $\gamma_{Q_2} \neq 1$). By varying γ_{Q_2} systematically, we can trace how the distortion modifies the balance between single-Q, double-Q, and SkX phases, while keeping all other parameters fixed.

The phase diagram is determined by large-scale Monte Carlo simulations based on simulated annealing. We use a lattice of $N = 16^2$ spins with periodic boundary conditions and employ standard Metropolis updates in real space. The simulation begins from random spin configurations at high temperature ($T/J_{Q_1} > 1$) and cools according to $T_{n+1} = \tilde{\alpha} T_n$, where $\tilde{\alpha} = 0.999995$–$0.999999$, until a final temperature $T = 0.01$ is reached, where thermal fluctuations can be negligible. Physical quantities are averaged over 10^5–10^6 Monte Carlo sweeps after equilibration, ensuring well-converged low-temperature states and reliable identification of phase boundaries.

The magnetic order is characterized by several quantities. The uniform magnetization along the field direction is defined as

$$M^z = \frac{1}{N} \sum_i S_i^z. \tag{2}$$

The spin correlations are analyzed via the spin structure factor,

$$S_s^\eta(\boldsymbol{q}) = \frac{1}{N} \sum_{i,j} S_i^\eta S_j^\eta e^{i\boldsymbol{q}\cdot(\boldsymbol{r}_i - \boldsymbol{r}_j)}, \qquad (\eta = x, y, z), \tag{3}$$

and the in-plane component is given by $S_s^{xy}(\boldsymbol{q}) = S_s^x(\boldsymbol{q}) + S_s^y(\boldsymbol{q})$. Here, $\boldsymbol{r}_i$ is the position vector at site i and $\boldsymbol{q}$ is the wave vector in the Brillouin zone. The amplitude of the magnetic Fourier mode is then

$$m_{\boldsymbol{q}}^\eta = \sqrt{\frac{S_s^\eta(\boldsymbol{q})}{N}}, \tag{4}$$

which distinguishes single-Q state from multiple-Q states. To capture the topological aspect of the spin textures, we evaluate the scalar spin chirality,

$$\chi^{\mathrm{sc}} = \frac{1}{N} \sum_i \sum_{\delta=\pm 1} \boldsymbol{S}_i \cdot (\boldsymbol{S}_{i+\delta\hat{x}} \times \boldsymbol{S}_{i+\delta\hat{y}}), \tag{5}$$

 doi:10.20944/preprints202602.0033.v1

where $\hat{x}$ and $\hat{y}$ denote unit translations along the x and y directions, respectively. A nonzero χ^{sc} identifies noncoplanar spin configurations such as SkXs, while its sign distinguishes the chirality of the underlying spin structure.

3. Results

We begin by mapping the low-temperature magnetic phase diagram in the (γ_{Q_2}, H) plane, as shown in Figure 1. Three primary phases are stabilized: a single-Q vertical spiral state denoted as 1Q VS at low fields, a double-Q SkX at intermediate fields, and a single-Q tilted conical spiral state denoted as 1Q TCS at higher fields approaching saturation. Another double-Q state also appears in a narrow region of the phase diagram at $\gamma_{Q_2} = 1$. As the uniaxial distortion increases (corresponding to smaller γ_{Q_2}), the SkX window narrows while single-Q phases expand, reflecting enhanced exchange anisotropy between the two orthogonal modulation channels $\boldsymbol{Q}_1$ and $\boldsymbol{Q}_2$.

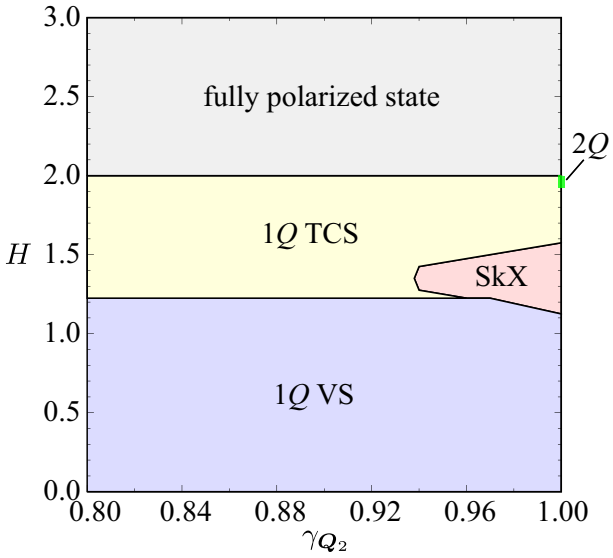

Figure 1. Magnetic phase diagram of the spin model described by Eq. (1) obtained at low temperature, highlighting the sequence of magnetic phase transitions driven by varying the interaction parameter at the ordering wave vector $\boldsymbol{Q}_2$, γ_{Q_2}, in the horizontal axis and the out-of-plane magnetic field, H, in the vertical axis. The other parameters are fixed to $J_{Q_1} = 1$ and $D = 0.3$. The labels 1Q and 2Q correspond to the single-Q and double-Q ordered states, respectively, whereas VS, TCS, and SkX denote the vertical spiral, tilted conical spiral, and skyrmion crystal phases.

Representative real-space spin textures at $\gamma_{Q_2} = 0.95$ are presented in Figure 2. In the single-Q vertical spiral state shown in Figure 2(a), the spins rotate within a plane containing the field axis to gain energy by the DM interaction, forming stripes with alternating S_i^z components and negligible in-plane vorticity. At intermediate fields, the system reorganizes into a square array of vortices and antivortices, constituting the SkX phase characterized by a finite scalar spin chirality χ^{sc}, as shown in Figure 2(b). At higher fields, the spin texture transforms into the single-Q tilted conical spiral texture, where a single helical modulation occurs in the xy plane, as shown in Figure 2(c). It is noted that the spiral plane of this state is slightly tilted from the xy plane to the zx plane owing to the presence of the DM interaction.

The corresponding spin structure factors in Figure 3 provide a clear reciprocal-space fingerprint of each magnetic phase. For both the single-Q vertical spiral and the tilted conical spiral states, the spectrum is dominated by a single pair of Bragg peaks at $\pm\boldsymbol{Q}_1$, reflecting a unidirectional helical modulation. In the single-Q vertical spiral phase, comparable intensities are found in the in-plane (S_s^{xy}) and out-of-plane (S_s^z) components, as shown in Figure 3(a), consistent with spins rotating within a plane that includes the magnetic-field direction. By contrast, in the single-Q tilted conical spiral state,

 doi:10.20944/preprints202602.0033.v1

the spectral weight in $S_s^z(\boldsymbol{Q}_1)$ is strongly suppressed while $S_s^{xy}(\boldsymbol{Q}_1)$ remains pronounced, as shown in Figure 3(c), indicating that the cone axis is slightly canted from the z direction.

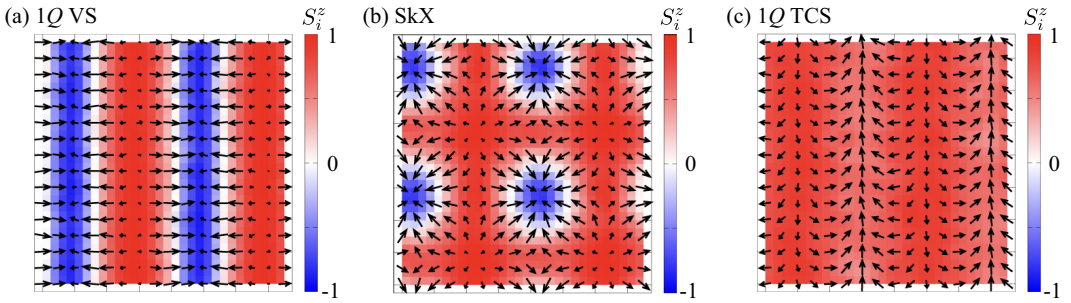

Figure 2. Real-space snapshots of spin configurations obtained from simulated annealing calculations. Panels (a)–(c) display representative magnetic textures at $\gamma_{Q_2} = 0.95$ for different magnetic fields: (a) the single-Q vertical spiral state at $H = 1$, (b) the skyrmion crystal at $H = 1.3$, and (c) the single-Q tilted conical spiral state at $H = 1.6$. Arrows indicate the local spin orientations, while the color scale represents the out-of-plane spin component S_i^z.

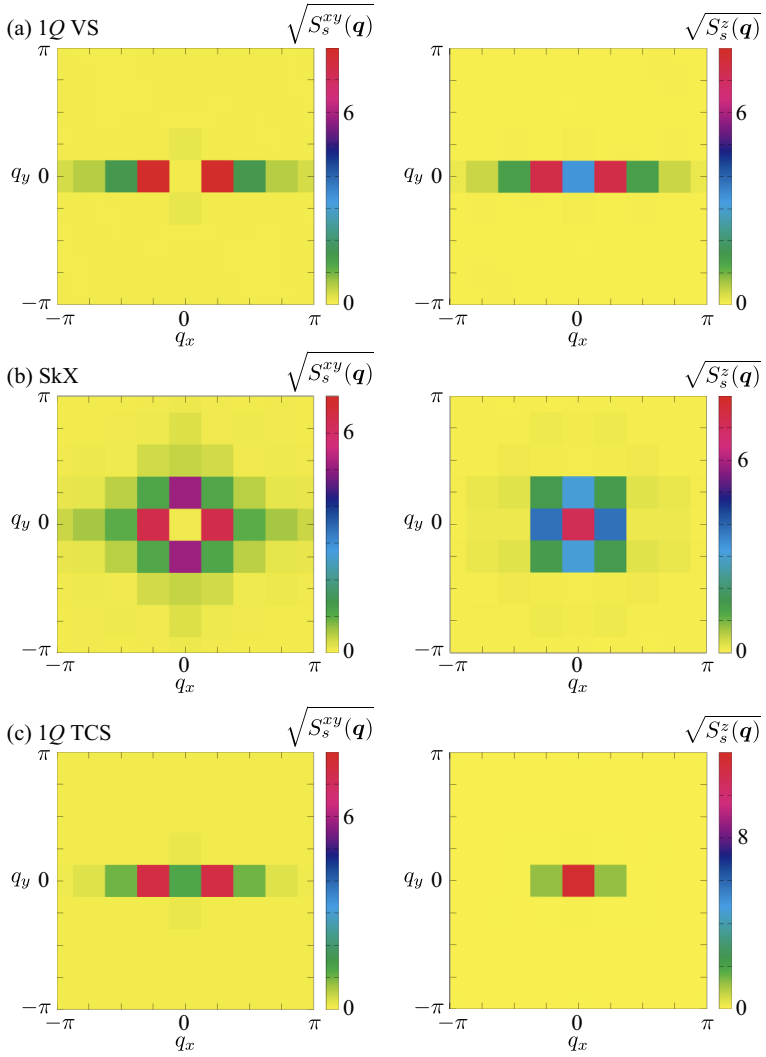

Figure 3. Square root of the spin structure factor for the magnetic states shown in Figure 2, whose peak patterns distinguish different magnetic phases. The left and right panels respectively display the intensity distributions for the in-plane $[S_s^{xy}(\boldsymbol{q})]$ and out-of-plane $[S_s^z(\boldsymbol{q})]$ spin components in momentum space.

In striking contrast, the SkX exhibits four principal Bragg peaks located at $\pm\boldsymbol{Q}_1$ and $\pm\boldsymbol{Q}_2$, which form a characteristic square pattern in reciprocal space that mirrors the real-space spin texture, as

 doi:10.20944/preprints202602.0033.v1

shown in Figure 3(b). Both $S_s^{xy}(\boldsymbol{q})$ and $S_s^{z}(\boldsymbol{q})$ display finite and comparable intensities at these ordering wave vectors, signifying that the spin texture contains substantial modulations in all three spin components. This spectral distribution evidences the superposition of two helical modes with orthogonal propagation vectors, giving rise to a noncoplanar double-Q spin configuration responsible for the finite scalar spin chirality and topological character of the SkX phase.

The evolution of these magnetic phases as a function of the magnetic field is summarized in Figures 4, 5, and 6 for different values of γ_{Q_2}. Each panel displays the field dependence of the uniform magnetization M^z in (a), the squared Fourier amplitudes of the spin moments $(m^{\eta}_{\boldsymbol{Q}_\nu})^2$ for $\eta = x, y, z$ in (b), and the squared scalar spin chirality $(\chi^{\rm sc})^2$ in (c). These quantities provide complementary insights into how the sequence of magnetic phases evolves with uniaxial distortion.

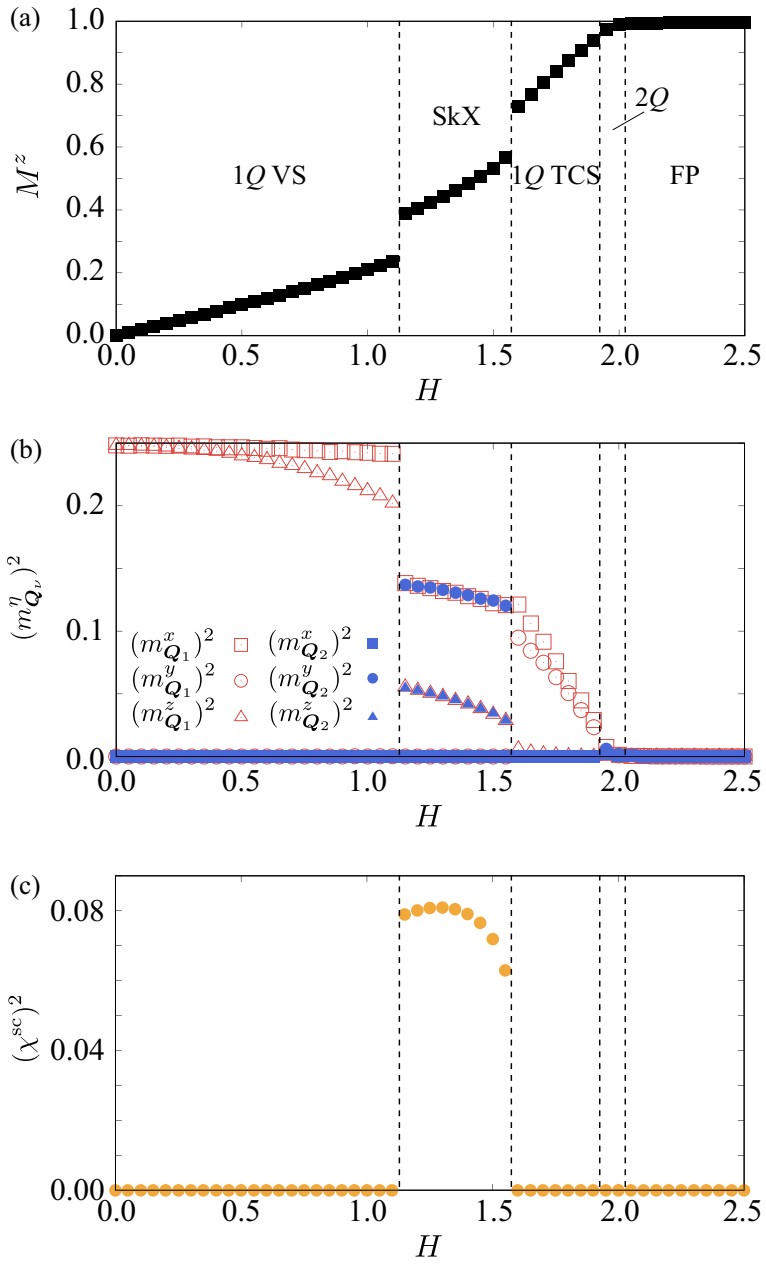

Figure 4. Magnetic-field dependence of characteristic quantities at $\gamma_{Q_2} = 1$. (a) Magnetization along the field direction, M^z; (b) squared magnetic moments $(m^{\eta}_{\boldsymbol{Q}_\nu})^2$ for the dominant ordering wave vectors; and (c) squared scalar spin chirality $(\chi^{\rm sc})^2$. The vertical dashed lines mark the phase boundaries separating distinct magnetic textures. FP stands for the fully polarized state.

 doi:10.20944/preprints202602.0033.v1

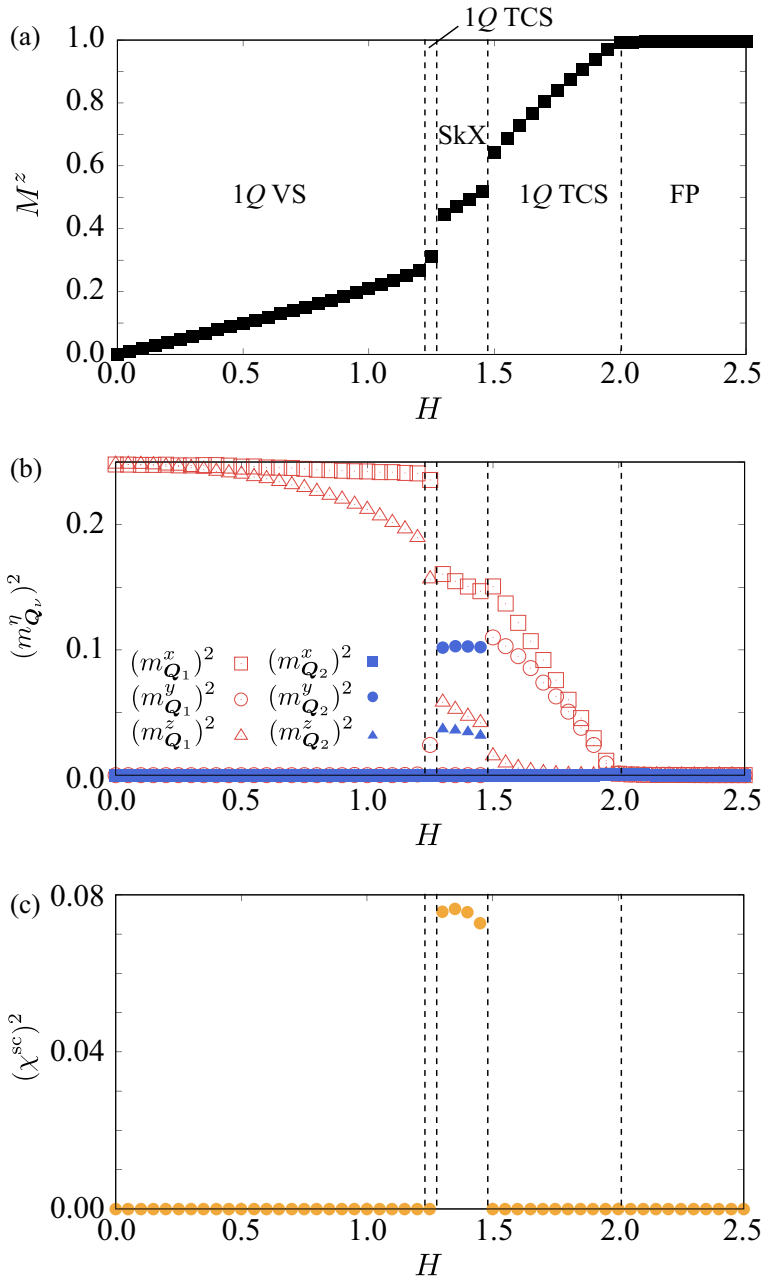

Figure 5. Magnetic-field dependence of characteristic quantities in terms of (a) M^z, (b) $(m^{\eta}_{Q_\nu})^2$, and (c) $(\chi^{sc})^2$, corresponding to Figure 4, at $\gamma_{Q_2} = 0.95$.

In the tetragonal limit, i.e.,$\gamma_{Q_2} = 1$, shown in Figure 4, five distinct regions appear as the magnetic field H increases. Figure 4(a) indicates that M^z grows in a stepwise manner with increasing field, reflecting successive phase transitions among the single-Q vertical spiral state, the SkX, the single-Q tilted conical spiral state, the double-Q state, and finally the fully polarized state. In the low-field region, the magnetization remains small, consistent with the nearly coplanar nature of the single-Q vertical spiral state. Upon entering the SkX phase, M^z exhibits a sudden enhancement, accompanied by partial alignment of the spins with the field due to the formation of vortex cores in the SkX phase. A further gradual increase in M^z occurs as the system transitions to the single-Q tilted conical spiral and double-Q states, where the conical and sinusoidal modulations are gradually suppressed by the Zeeman energy. Figure 4(b) shows the corresponding evolution of the order parameters: in the single-Q vertical spiral phase, the Fourier weights in the in-plane $m^{x,y}_{Q_1}$ and out-of-plane $m^z_{Q_1}$ components are almost the same. The magnitude of $m^z_{Q_1}$ becomes smaller while increasing H, since the spins tend to align along the perpendicular direction of the magnetic field to gain the energy by J_{Q_1}. Entering

 doi:10.20944/preprints202602.0033.v1

the SkX region, finite components at both $\boldsymbol{Q}_1$ and $\boldsymbol{Q}_2$ emerge in all spin directions, confirming the superposition of two orthogonal modulations that produce a noncoplanar spin texture. At higher fields, the in-plane components $m^{x,y}_{\boldsymbol{Q}_\nu}$ dominate. Figure 4(c) highlights the field dependence of the squared scalar spin chirality $(\chi^{\rm sc})^2$: it is zero in the single-Q vertical spiral phase, exhibits a pronounced plateau-like behavior in the SkX regime, signaling robust topological order, and vanishes again in the single-Q tilted conical spiral, the double-Q, and fully polarized states. These combined trends establish that the SkX appears only in a limited field window surrounded by topologically trivial spiral states.

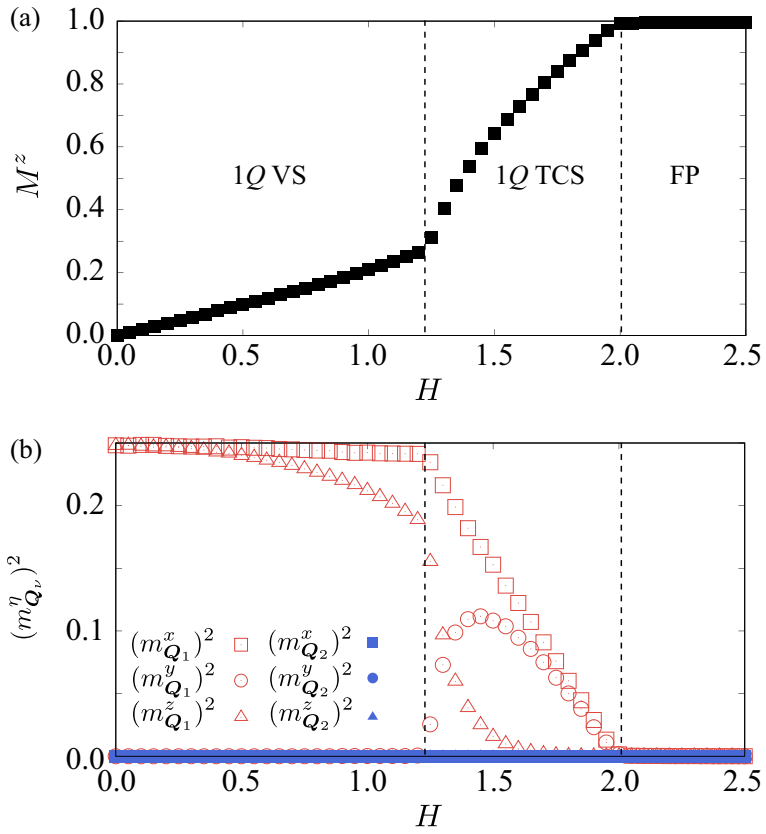

Figure 6. Magnetic-field dependence of characteristic quantities in terms of (a) M^z and (b) $(m^\eta_{\boldsymbol{Q}_\nu})^2$, corresponding to Figure 4, at $\gamma_{\boldsymbol{Q}_2} = 0.9$.

Figure 5 presents the corresponding results for moderate uniaxial distortion at $\gamma_{\boldsymbol{Q}_2} = 0.95$. Similarly to the case of $\gamma_{\boldsymbol{Q}_2} = 1$, the magnetic field evolution in Figure 5(a) shows stepwise changes in M^z, but the range of the SkX phase becomes narrower than in the tetragonal limit. An additional single-Q tilted conical spiral phase intervenes between the single-Q vertical spiral and SkX regions, suggesting that the anisotropy between $\boldsymbol{Q}_1$ and $\boldsymbol{Q}_2$ channels partially suppresses the double-Q interference essential for stabilizing the SkX. In Figure 5(b), the reduction of the $\boldsymbol{Q}_2$ component is evident: $m^{x,y}_{\boldsymbol{Q}_2}$ and $m^z_{\boldsymbol{Q}_2}$ acquire smaller amplitudes than their $\boldsymbol{Q}_1$ counterparts, producing an asymmetric intensity distribution in momentum space that mirrors the twofold distortion in real space. Nevertheless, within a narrow field window, the SkX retains finite contributions from both $\boldsymbol{Q}_1$ and $\boldsymbol{Q}_2$, maintaining its topological character. Figure 5(c) further confirms this behavior: $(\chi^{\rm sc})^2$ develops a distinct but narrower plateau compared with Figure 4(c), indicating that the SkX remains stable only within a limited field range before being replaced by a topologically trivial single-Q tilted conical spiral state at higher fields. This result demonstrates that a modest ($\sim$5%) anisotropy already leads to substantial deformation of the SkX and reduction of its stability window.

For stronger uniaxial distortion at $\gamma_{\boldsymbol{Q}_2} = 0.9$, the results in Figure 6 show that the SkX phase is completely suppressed. Figure 6(a) reveals a smoother and more monotonic increase in magnetization without distinct jumps, consistent with continuous evolution from the single-Q vertical spiral state to the single-Q tilted conical spiral state, and then to the fully polarized state. Figure 6(b) exhibits a single

 doi:10.20944/preprints202602.0033.v1

dominant Fourier component at $\boldsymbol{Q}_1$ throughout the field range; the secondary $\boldsymbol{Q}_2$ mode is completely absent, signifying the collapse of double-Q superposition. Both $m^z_{\boldsymbol{Q}_1}$ and $m^{x,y}_{\boldsymbol{Q}_1}$ gradually decrease. The small decrease of $m^{x,y}_{\boldsymbol{Q}_1}$ compared to $m^z_{\boldsymbol{Q}_1}$ reflects the tendency of the spin flop in terms of the field direction. $(\chi^{\rm sc})^2$ remains vanishingly small over the entire field range (not shown), which means the topologically trivial nature of these states. These results collectively establish that increasing distortion systematically suppresses the noncoplanar SkX and double-Q phases, favoring simpler single-Q spiral textures whose ordering wave vector aligns with the distortion axis.

Figure 7 presents the $\gamma_{\boldsymbol{Q}_2}$ dependence of the squared magnetic Fourier components $(m^\eta_{\boldsymbol{Q}_\nu})^2$ at three representative magnetic fields, $H = 1$, 1.3, and 1.6, which correspond respectively to the single-Q vertical spiral state, the SkX, and the single-Q tilted conical spiral state at $\gamma_{\boldsymbol{Q}_2} = 1$. These results reveal in detail how uniaxial distortion, represented by the deviation of $\gamma_{\boldsymbol{Q}_2}$ from unity, continuously modifies the relative intensities of the two ordering wave vectors $\boldsymbol{Q}_1$ and $\boldsymbol{Q}_2$ and thereby controls the stability of each spiral structure.

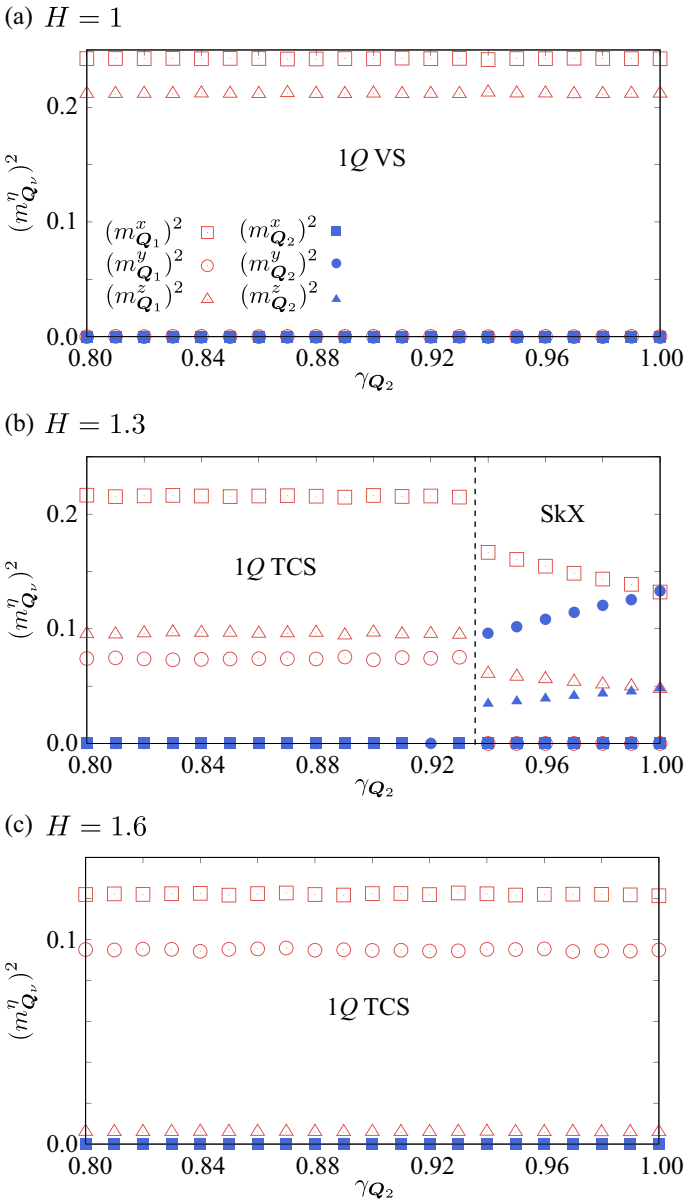

Figure 7. Dependence of the squared magnetic moments $(m^\eta_{\boldsymbol{Q}_\nu})^2$ on the interaction ratio $\gamma_{\boldsymbol{Q}_2}$ at different magnetic fields: (a) $H = 1$, (b) $H = 1.3$, and (c) $H = 1.6$. The vertical dashed line indicates the phase boundary between the single-Q tilted conical spiral state and the skyrmion crystal.

 doi:10.20944/preprints202602.0033.v1

In the case of $H = 1$ in Figure 7(a), the system resides in the single-Q vertical spiral phase irrespective of the magnitude of distortion. The dominant Fourier components $(m^x_{Q_1})^2$ and $(m^z_{Q_1})^2$ exhibit almost no dependence on γ_{Q_2}. This is because the change of γ_{Q_2} does not affect the internal energy of the single-Q vertical spiral phase. Similarly, the single-Q tilted conical spiral state remains stable against distortion, as shown in Figure 7(c).

Meanwhile, in the region where the SkX phase is stabilized in the absence of distortion at $H = 1.3$ in Figure 7(b), there is a clear topological phase transition driven by the variation of γ_{Q_2}. Upon decreasing γ_{Q_2}, the Fourier amplitudes associated with $\boldsymbol{Q}_2$ systematically decrease, while those at $\boldsymbol{Q}_1$ are gradually enhanced. The imbalance between the two modulation wave vectors grows continuously, signaling that the uniaxial distortion suppresses the interference between the orthogonal spiral components. At a critical value of $\gamma_{Q_2} \simeq 0.93$, the $\boldsymbol{Q}_2$ contribution vanishes, and the system transitions into the single-Q tilted conical spiral state, as indicated by the vertical dashed line in Figure 7(b). This behavior demonstrates that even a modest uniaxial anisotropy is sufficient to destabilize the SkX by lifting the degeneracy between $\boldsymbol{Q}_1$ and $\boldsymbol{Q}_2$. The corresponding evolution of the topological property is captured in Figure 8, which displays the γ_{Q_2} dependence of the squared scalar spin chirality $(\chi^{\rm sc})^2$ at the same field of $H = 1.3$. As γ_{Q_2} decreases, $(\chi^{\rm sc})^2$ sharply drops to zero according to the transition to the single-Q tilted conical spiral state.

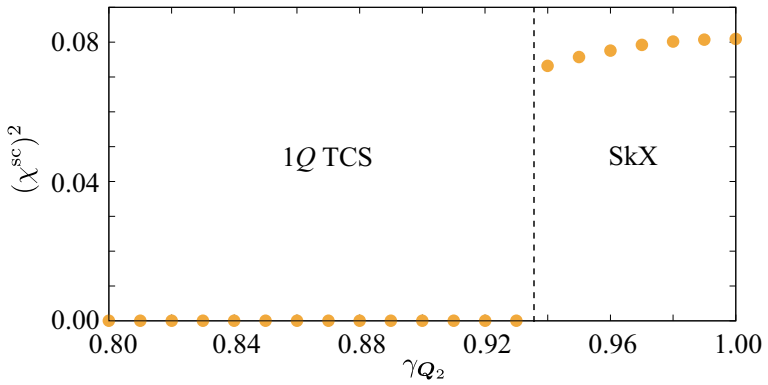

Figure 8. Dependence of the squared scalar spin chirality $(\chi^{\rm sc})^2$ on γ_{Q_2} at $H = 1.3$. The vertical dashed line indicates the phase boundary between the single-Q tilted conical spiral state and the skyrmion crystal.

Next, we discuss the stability of the SkX under distortion for different values of the DM interaction. Figures 9(a) and 9(b) show the low-temperature magnetic phase diagrams in the γ_{Q_2}–H plane for $D = 0.1$ and $D = 0.5$, respectively. For the weaker DM interaction $D = 0.1$, three phases are stabilized: the single-Q vertical spiral state at low magnetic fields, the single-Q tilted conical spiral state at intermediate fields, and the fully polarized state at high fields, as shown in Figure 9(a); the SkX does not appear in the phase diagram. Since both the single-Q vertical spiral and tilted conical spiral states are characterized by the single-Q peak structure at $\boldsymbol{Q}_1$, the change of γ_{Q_2} does not alter their stability. The phase boundaries do not depend on γ_{Q_2}.

In contrast, for the stronger DM interaction $D = 0.5$, the SkX region dramatically expands both in γ_{Q_2} and H, forming a robust pocket bounded by the single-Q vertical spiral and single-Q tilted conical spiral phases, as shown in Figure 9(b). This comparison clearly demonstrates that increasing D enhances the energetic stability of the SkX and compensates for the anisotropy introduced by the uniaxial distortion, thereby broadening the region where the double-Q spin configuration is stabilized.

The real-space spin configurations corresponding to the SkX at different degrees of distortion are illustrated in Figure 10 for $H = 1.7$. In the absence of distortion ($\gamma_{Q_2} = 1$) in Figure 10(a), the SkX forms a perfectly symmetric square array of skyrmions, with nearly circular cores and uniform periodicity. At $\gamma_{Q_2} = 0.95$ shown in Figure 10(b), the SkX remains topologically intact but exhibits a weak elongation along the distortion axis, and the skyrmion cores deform into slightly elliptical shapes. With further distortion at $\gamma_{Q_2} = 0.88$ in Figure 10(c) and $\gamma_{Q_2} = 0.81$ in Figure 10(d), the anisotropy

 doi:10.20944/preprints202602.0033.v1

becomes more pronounced, and the lattice transforms into a rectangular arrangement with compressed cores along the Q_2 direction.

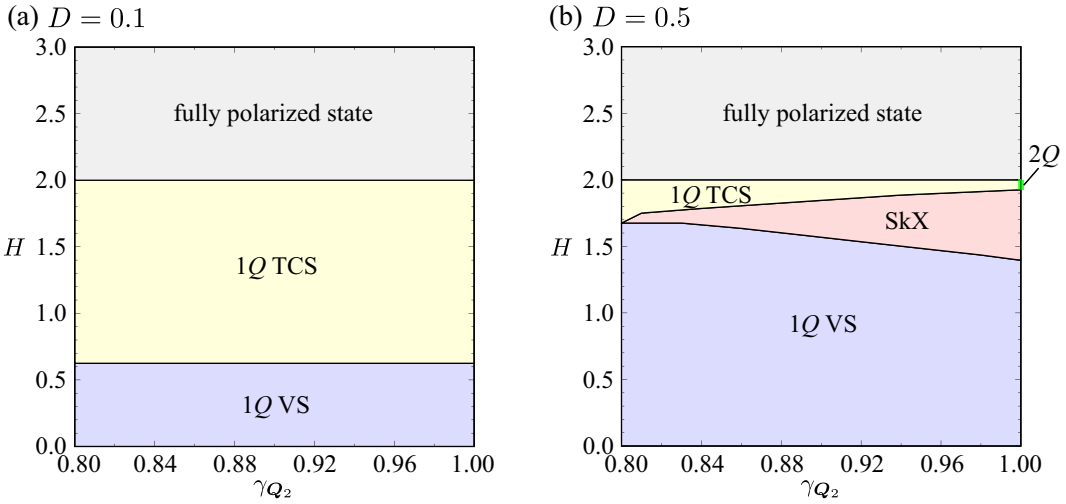

Figure 9. Magnetic phase diagrams in the γ_{Q_2}–H plane at (a) $D = 0.1$ and (b) $D = 0.5$. The labels 1Q and 2Q correspond to the single-Q and double-Q ordered states, respectively, whereas VS, TCS, and SkX denote the vertical spiral, tilted conical spiral, and skyrmion crystal phases.

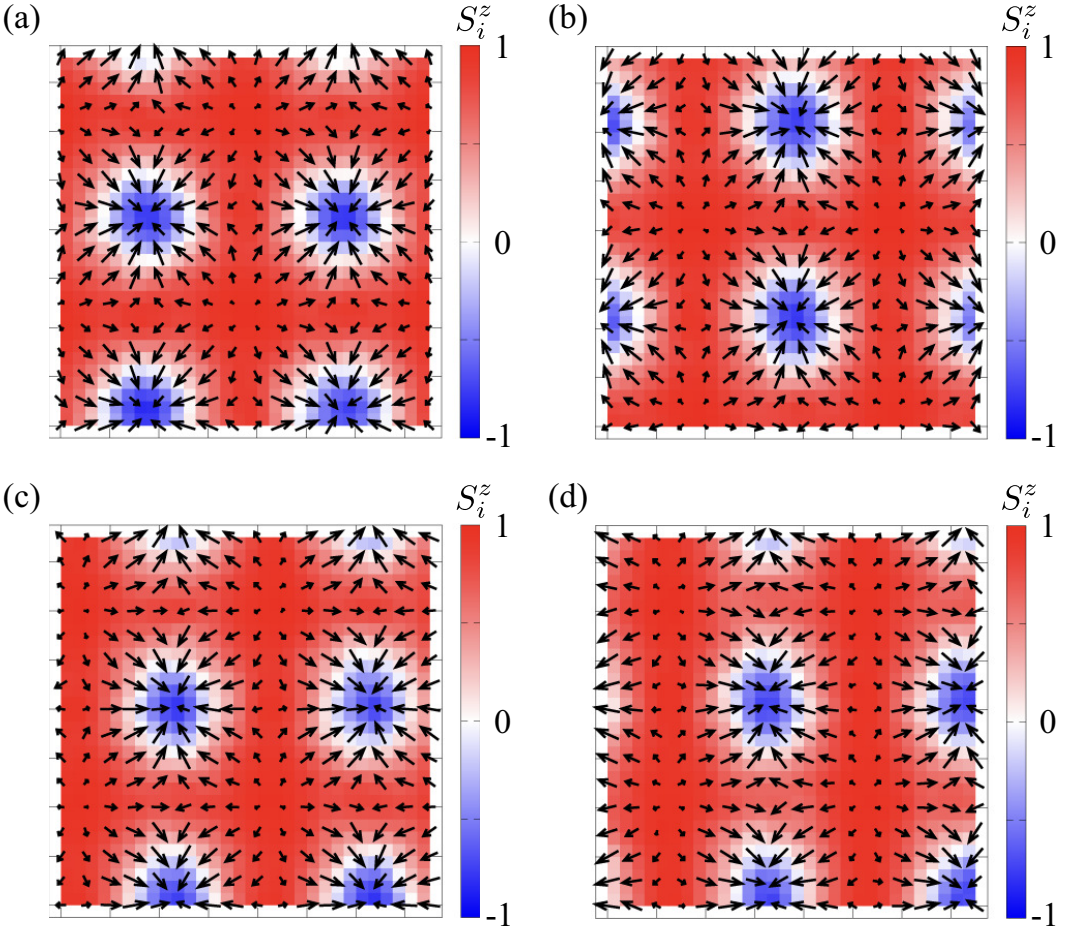

Figure 10. Real-space snapshots of spin configurations in the skyrmion crystal phases at (a) $\gamma_{Q_2} = 1$, (b) $\gamma_{Q_2} = 0.95$, (c) $\gamma_{Q_2} = 0.88$, and (d) $\gamma_{Q_2} = 0.81$ for $H = 1.7$. Arrows indicate the local spin orientations, while the color scale represents the out-of-plane spin component S_i^z.

Figure 11 further quantifies this distortion-driven evolution at $H = 1.7$ by showing the γ_{Q_2} dependence of the squared Fourier amplitudes $(m^{\eta}_{Q_\nu})^2$ and the squared scalar spin chirality $(\chi^{\rm sc})^2$.

 doi:10.20944/preprints202602.0033.v1

In Figure 11(a), the $\boldsymbol{Q}_2$ components gradually decrease as $\gamma_{\boldsymbol{Q}_2}$ is reduced, while the $\boldsymbol{Q}_1$ components are slightly enhanced, illustrating the imbalance between the two modulation directions. The vertical dashed line denotes the critical distortion where the $\boldsymbol{Q}_2$ amplitude nearly vanishes, signaling the transition from the SkX to the single-Q tilted conical spiral phase. In Figure 11(b), $(\chi^{\rm sc})^2$ exhibits finite values, reflecting the stable topological SkX, but rapidly drops to zero around $\gamma_{\boldsymbol{Q}_2} \approx 0.8$. The concurrent disappearance of the $\boldsymbol{Q}_2$ mode and $(\chi^{\rm sc})^2$ demonstrates that uniaxial distortion induces a topological phase transition from the SkX to the single-Q tilted conical spiral state. These results show that the cooperative effect of DM interaction and exchange anisotropy on the formation and suppression of the double-Q SkX.

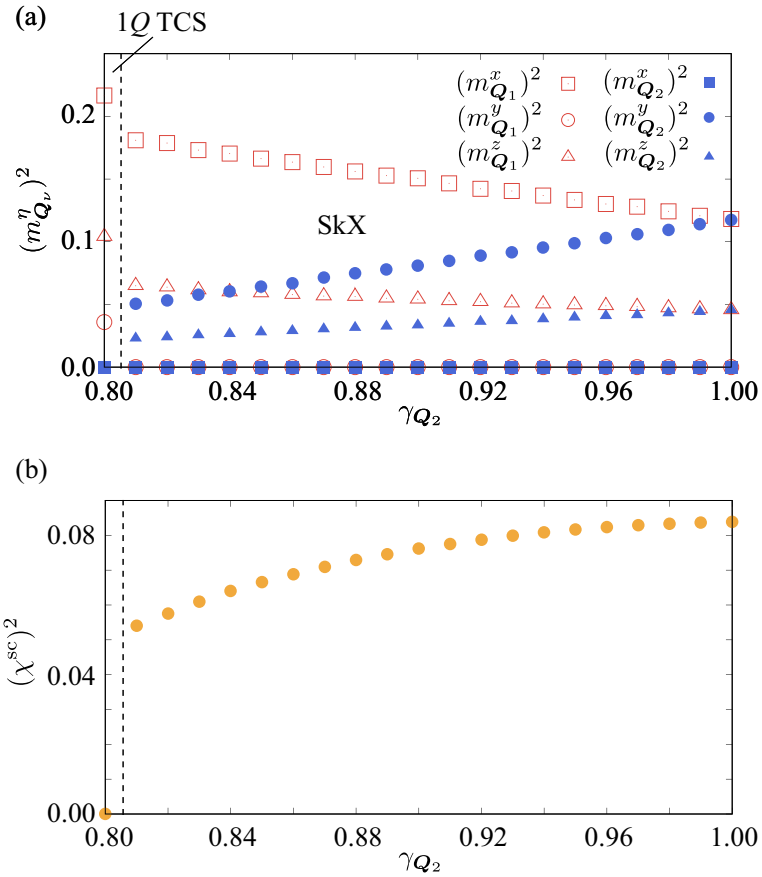

Figure 11. Dependence of (a) the squared magnetic moments $(m^\eta_{\boldsymbol{Q}_\nu})^2$ on the interaction ratio $\gamma_{\boldsymbol{Q}_2}$ and (b) the squared scalar spin chirality $(\chi^{\rm sc})^2$ at $H = 1.7$. The vertical dashed line indicates the phase boundary between the single-Q tilted conical spiral state and the skyrmion crystal.

4. Conclusions

We have theoretically investigated the effects of uniaxial distortion on the stability of the square SkX in noncentrosymmetric tetragonal magnets by analyzing a classical spin model that incorporates momentum-resolved frustrated interactions and DM interactions. Using simulated-annealing calculations, we clarified how the interplay between exchange anisotropy and DM interaction governs the formation, deformation, and collapse of topological spin textures.

The results revealed that in the absence of distortion, the double-Q SkX phase emerges between the single-Q vertical spiral state and the single-Q tilted conical spiral state in the intermediate magnetic-field region. As uniaxial distortion is introduced, the equivalence between the two ordering wave vectors $\boldsymbol{Q}_1$ and $\boldsymbol{Q}_2$ is lifted, suppressing the interference between the orthogonal spiral components. This effect continuously weakens the noncoplanar modulation characteristic of the SkX, and beyond a critical anisotropy ratio $\gamma_{\boldsymbol{Q}_2} \sim 0.93$, the $\boldsymbol{Q}_2$ contribution vanishes, driving a topological phase transition from the SkX to the single-Q tilted conical spiral phase. The concomitant disappearance of

 doi:10.20944/preprints202602.0033.v1

the scalar spin chirality confirms that this transition involves a change from a topologically nontrivial to a trivial spin texture.

Furthermore, by systematically varying the magnitude of the DM interaction, we demonstrated that the stability region of the SkX strongly depends on D. For weak DM interaction, only single-Q spiral states are stabilized. Meanwhile, when the DM interaction is further increased, the SkX region expands substantially in both magnetic field and anisotropy range, highlighting the cooperative role of the DM interaction in compensating the exchange anisotropy induced by distortion. The real-space spin textures and reciprocal-space spin structure factors consistently reflect these trends, showing the deformation and eventual collapse of the SkX as the uniaxial distortion strengthens. Our study establishes a unified understanding of how strain and DM interactions interplay to control the stability of square SkXs in noncentrosymmetric magnets.

Funding: This research was supported by JSPS KAKENHI Grants Numbers JP22H00101, JP22H01183, JP23H04869, JP23K03288, JP23K20827, and by JST CREST (JPMJCR23O4) and JST FOREST (JPMJFR2366).

Data Availability Statement: The original contributions presented in the study are included in the article, further inquiries can be directed to the corresponding author.

References

1. Skyrme, T. A non-linear field theory. *Proc. Roy. Soc* **1961**, *260*, 127.
2. Skyrme, T.H.R. A unified field theory of mesons and baryons. *Nucl. Phys.* **1962**, *31*, 556–569.
3. Wright, D.C.; Mermin, N.D. Crystalline liquids: the blue phases. *Rev. Mod. Phys.* **1989**, *61*, 385–432. https://doi.org/10.1103/RevModPhys.61.385.
4. Leonov, A.O.; Dragunov, I.E.; Rößler, U.K.; Bogdanov, A.N. Theory of skyrmion states in liquid crystals. *Phys. Rev. E* **2014**, *90*, 042502. https://doi.org/10.1103/PhysRevE.90.042502.
5. Afghah, S.; Selinger, J.V. Theory of helicoids and skyrmions in confined cholesteric liquid crystals. *Phys. Rev. E* **2017**, *96*, 012708. https://doi.org/10.1103/PhysRevE.96.012708.
6. Duzgun, A.; Selinger, J.V.; Saxena, A. Comparing skyrmions and merons in chiral liquid crystals and magnets. *Phys. Rev. E* **2018**, *97*, 062706. https://doi.org/10.1103/PhysRevE.97.062706.
7. Duzgun, A.; Nisoli, C. Skyrmion Spin Ice in Liquid Crystals. *Phys. Rev. Lett.* **2021**, *126*, 047801. https://doi.org/10.1103/PhysRevLett.126.047801.
8. Sondhi, S.L.; Karlhede, A.; Kivelson, S.A.; Rezayi, E.H. Skyrmions and the crossover from the integer to fractional quantum Hall effect at small Zeeman energies. *Phys. Rev. B* **1993**, *47*, 16419–16426. https://doi.org/10.1103/PhysRevB.47.16419.
9. Abolfath, M.; Palacios, J.J.; Fertig, H.A.; Girvin, S.M.; MacDonald, A.H. Critical comparison of classical field theory and microscopic wave functions for skyrmions in quantum Hall ferromagnets. *Phys. Rev. B* **1997**, *56*, 6795–6804. https://doi.org/10.1103/PhysRevB.56.6795.
10. Xie, X.C.; He, S. Skyrmion excitations in quantum Hall systems. *Phys. Rev. B* **1996**, *53*, 1046–1049. https://doi.org/10.1103/PhysRevB.53.1046.
11. Stone, M. Magnus force on skyrmions in ferromagnets and quantum Hall systems. *Phys. Rev. B* **1996**, *53*, 16573–16578. https://doi.org/10.1103/PhysRevB.53.16573.
12. Fertig, H.A.; Brey, L.; Côté, R.; MacDonald, A.H.; Karlhede, A.; Sondhi, S.L. Hartree-Fock theory of Skyrmions in quantum Hall ferromagnets. *Phys. Rev. B* **1997**, *55*, 10671–10680. https://doi.org/10.1103/PhysRevB.55.10671.
13. Shkolnikov, Y.P.; Misra, S.; Bishop, N.C.; De Poortere, E.P.; Shayegan, M. Observation of Quantum Hall "Valley Skyrmions". *Phys. Rev. Lett.* **2005**, *95*, 066809. https://doi.org/10.1103/PhysRevLett.95.066809.
14. Yang, K.; Das Sarma, S.; MacDonald, A.H. Collective modes and skyrmion excitations in graphene $SU(4)$ quantum Hall ferromagnets. *Phys. Rev. B* **2006**, *74*, 075423. https://doi.org/10.1103/PhysRevB.74.075423.
15. Ho, T.L. Spinor Bose Condensates in Optical Traps. *Phys. Rev. Lett.* **1998**, *81*, 742–745. https://doi.org/10.1103/PhysRevLett.81.742.
16. Al Khawaja, U.; Stoof, H. Skyrmions in a ferromagnetic Bose-Einstein condensate. *Nature* **2001**, *411*, 918–920. https://doi.org/https://doi.org/10.1038/35082010.
17. Khawaja, U.A.; Stoof, H.T.C. Skyrmion physics in Bose-Einstein ferromagnets. *Phys. Rev. A* **2001**, *64*, 043612. https://doi.org/10.1103/PhysRevA.64.043612.

 doi:10.20944/preprints202602.0033.v1

18. Ruostekoski, J.; Anglin, J.R. Creating Vortex Rings and Three-Dimensional Skyrmions in Bose-Einstein Condensates. *Phys. Rev. Lett.* **2001**, *86*, 3934–3937. https://doi.org/10.1103/PhysRevLett.86.3934.
19. Battye, R.A.; Cooper, N.R.; Sutcliffe, P.M. Stable Skyrmions in Two-Component Bose-Einstein Condensates. *Phys. Rev. Lett.* **2002**, *88*, 080401. https://doi.org/10.1103/PhysRevLett.88.080401.
20. Savage, C.M.; Ruostekoski, J. Energetically Stable Particlelike Skyrmions in a Trapped Bose-Einstein Condensate. *Phys. Rev. Lett.* **2003**, *91*, 010403. https://doi.org/10.1103/PhysRevLett.91.010403.
21. Das, S.; Tang, Y.; Hong, Z.; Gonçalves, M.; McCarter, M.; Klewe, C.; Nguyen, K.; Gómez-Ortiz, F.; Shafer, P.; Arenholz, E.; et al. Observation of room-temperature polar skyrmions. *Nature* **2019**, *568*, 368–372. https://doi.org/https://doi.org/10.1038/s41586-019-1092-8.
22. McCarter, M.R.; Kim, K.T.; Stoica, V.A.; Das, S.; Klewe, C.; Donoway, E.P.; Burn, D.M.; Shafer, P.; Rodolakis, F.; Gonçalves, M.A.P.; et al. Structural Chirality of Polar Skyrmions Probed by Resonant Elastic X-Ray Scattering. *Phys. Rev. Lett.* **2022**, *129*, 247601. https://doi.org/10.1103/PhysRevLett.129.247601.
23. Yuan, S.; Chen, Z.; Prokhorenko, S.; Nahas, Y.; Bellaiche, L.; Liu, C.; Xu, B.; Chen, L.; Das, S.; Martin, L.W. Hexagonal Close-Packed Polar-Skyrmion Lattice in Ultrathin Ferroelectric $PbTiO_3$ Films. *Phys. Rev. Lett.* **2023**, *130*, 226801. https://doi.org/10.1103/PhysRevLett.130.226801.
24. Kong, L.; Tang, J.; Wu, Y.; Wang, W.; Jiang, J.; Wang, Y.; Li, J.; Xiong, Y.; Wang, S.; Tian, M.; et al. Diverse helicities of dipolar skyrmions. *Phys. Rev. B* **2024**, *109*, 014401. https://doi.org/10.1103/PhysRevB.109.014401.
25. Xue, F.; Zhang, C.; Zheng, S.; Tong, P.; Wang, B.; Peng, Y.; Wang, Z.; Xu, H.; He, Y.; Zhou, H.; et al. Observation of switchable polar skyrmion bubbles down to the atomic layers in van der Waals ferroelectric $CuInP_2S_6$. *Nat. Commun.* **2025**, *16*, 2349. https://doi.org/https://doi.org/10.1038/s41467-025-57714-9.
26. Bogdanov, A.N.; Yablonskii, D.A. Thermodynamically stable "vortices" in magnetically ordered crystals: The mixed state of magnets. *Sov. Phys. JETP* **1989**, *68*, 101.
27. Bogdanov, A.; Hubert, A. Thermodynamically stable magnetic vortex states in magnetic crystals. *J. Magn. Magn. Mater.* **1994**, *138*, 255 – 269. https://doi.org/http://dx.doi.org/10.1016/0304-8853(94)90046-9.
28. Ishikawa, Y.; Tajima, K.; Bloch, D.; Roth, M. Helical spin structure in manganese silicide MnSi. *Solid State Commun.* **1976**, *19*, 525–528. https://doi.org/https://doi.org/10.1016/0038-1098(76)90057-0.
29. Mühlbauer, S.; Binz, B.; Jonietz, F.; Pfleiderer, C.; Rosch, A.; Neubauer, A.; Georgii, R.; Böni, P. Skyrmion lattice in a chiral magnet. *Science* **2009**, *323*, 915–919. https://doi.org/10.1126/science.1166767.
30. Neubauer, A.; Pfleiderer, C.; Binz, B.; Rosch, A.; Ritz, R.; Niklowitz, P.G.; Böni, P. Topological Hall Effect in the *A* Phase of MnSi. *Phys. Rev. Lett.* **2009**, *102*, 186602. https://doi.org/10.1103/PhysRevLett.102.186602.
31. Yu, X.Z.; Onose, Y.; Kanazawa, N.; Park, J.H.; Han, J.H.; Matsui, Y.; Nagaosa, N.; Tokura, Y. Real-space observation of a two-dimensional skyrmion crystal. *Nature* **2010**, *465*, 901–904. https://doi.org/10.1038/nature09124.
32. Beille, J.; Voiron, J.; Roth, M. Long period helimagnetism in the cubic B20 $Fe_xCo_{1-x}Si$ and Co_xMn_{1-x} Si alloys. *Solid State Commun.* **1983**, *47*, 399–402. https://doi.org/10.1016/0038-1098(83)90928-6.
33. Yu, X.Z.; Kanazawa, N.; Onose, Y.; Kimoto, K.; Zhang, W.; Ishiwata, S.; Matsui, Y.; Tokura, Y. Near room-temperature formation of a skyrmion crystal in thin-films of the helimagnet FeGe. *Nat. Mater.* **2011**, *10*, 106–109. https://doi.org/10.1038/nmat2916.
34. Lebech, B.; Bernhard, J.; Freltoft, T. Magnetic structures of cubic FeGe studied by small-angle neutron scattering. *J. Phys.: Condens. Matter* **1989**, *1*, 6105. https://doi.org/10.1088/0953-8984/1/35/010.
35. Seki, S.; Yu, X.Z.; Ishiwata, S.; Tokura, Y. Observation of skyrmions in a multiferroic material. *Science* **2012**, *336*, 198–201. https://doi.org/10.1126/science.1214143.
36. Adams, T.; Chacon, A.; Wagner, M.; Bauer, A.; Brandl, G.; Pedersen, B.; Berger, H.; Lemmens, P.; Pfleiderer, C. Long-Wavelength Helimagnetic Order and Skyrmion Lattice Phase in Cu_2OSeO_3. *Phys. Rev. Lett.* **2012**, *108*, 237204. https://doi.org/10.1103/PhysRevLett.108.237204.
37. Seki, S.; Kim, J.H.; Inosov, D.S.; Georgii, R.; Keimer, B.; Ishiwata, S.; Tokura, Y. Formation and rotation of skyrmion crystal in the chiral-lattice insulator Cu_2OSeO_3. *Phys. Rev. B* **2012**, *85*, 220406. https://doi.org/10.1103/PhysRevB.85.220406.
38. Fert, A.; Cros, V.; Sampaio, J. Skyrmions on the track. *Nat. Nanotechnol.* **2013**, *8*, 152. https://doi.org/10.1038/nnano.2013.29.
39. Kang, W.; Huang, Y.; Zhang, X.; Zhou, Y.; Zhao, W. Skyrmion-electronics: An overview and outlook. *Proc. IEEE* **2016**, *104*, 2040–2061. https://doi.org/10.1109/JPROC.2016.2591578.
40. Finocchio, G.; Büttner, F.; Tomasello, R.; Carpentieri, M.; Kläui, M. Magnetic skyrmions: from fundamental to applications. *J. Phys. D: Appl. Phys.* **2016**, *49*, 423001. https://doi.org/10.1088/0022-3727/49/42/423001.

 doi:10.20944/preprints202602.0033.v1

41. Fert, A.; Reyren, N.; Cros, V. Magnetic skyrmions: advances in physics and potential applications. *Nat. Rev. Mater.* **2017**, *2*, 17031. https://doi.org/10.1038/natrevmats.2017.31.
42. Zhang, X.; Zhou, Y.; Song, K.M.; Park, T.E.; Xia, J.; Ezawa, M.; Liu, X.; Zhao, W.; Zhao, G.; Woo, S. Skyrmion-electronics: writing, deleting, reading and processing magnetic skyrmions toward spintronic applications. *J. Phys.: Condens. Matter* **2020**, *32*, 143001. https://doi.org/10.1088/1361-648X/ab5488.
43. Bogdanov, A.N.; Panagopoulos, C. Physical foundations and basic properties of magnetic skyrmions. *Nat. Rev. Phys.* **2020**, *2*, 492–498. https://doi.org/https://doi.org/10.1038/s42254-020-0203-7.
44. Reichhardt, C.; Reichhardt, C.J.O.; Milošević, M.V. Statics and dynamics of skyrmions interacting with disorder and nanostructures. *Rev. Mod. Phys.* **2022**, *94*, 035005. https://doi.org/10.1103/RevModPhys.94.035005.
45. Dzyaloshinsky, I. A thermodynamic theory of "weak" ferromagnetism of antiferromagnetics. *J. Phys. Chem. Solids* **1958**, *4*, 241–255.
46. Moriya, T. Anisotropic superexchange interaction and weak ferromagnetism. *Phys. Rev.* **1960**, *120*, 91. https://doi.org/https://doi.org/10.1103/PhysRev.120.91.
47. Rößler, U.K.; Bogdanov, A.N.; Pfleiderer, C. Spontaneous skyrmion ground states in magnetic metals. *Nature* **2006**, *442*, 797–801. https://doi.org/10.1038/nature05056.
48. Heinze, S.; von Bergmann, K.; Menzel, M.; Brede, J.; Kubetzka, A.; Wiesendanger, R.; Bihlmayer, G.; Blügel, S. Spontaneous atomic-scale magnetic skyrmion lattice in two dimensions. *Nat. Phys.* **2011**, *7*, 713–718. https://doi.org/10.1038/nphys2045.
49. Nagaosa, N.; Tokura, Y. Topological properties and dynamics of magnetic skyrmions. *Nat. Nanotechnol.* **2013**, *8*, 899–911. https://doi.org/10.1038/nnano.2013.243.
50. Tokura, Y.; Kanazawa, N. Magnetic Skyrmion Materials. *Chem. Rev.* **2021**, *121*, 2857. https://doi.org/10.1021/acs.chemrev.0c00297.
51. Loss, D.; Goldbart, P.M. Persistent currents from Berry's phase in mesoscopic systems. *Phys. Rev. B* **1992**, *45*, 13544–13561. https://doi.org/10.1103/PhysRevB.45.13544.
52. Ye, J.; Kim, Y.B.; Millis, A.J.; Shraiman, B.I.; Majumdar, P.; Tešanović, Z. Berry Phase Theory of the Anomalous Hall Effect: Application to Colossal Magnetoresistance Manganites. *Phys. Rev. Lett.* **1999**, *83*, 3737–3740. https://doi.org/10.1103/PhysRevLett.83.3737.
53. Ohgushi, K.; Murakami, S.; Nagaosa, N. Spin anisotropy and quantum Hall effect in the *kagomé* lattice: Chiral spin state based on a ferromagnet. *Phys. Rev. B* **2000**, *62*, R6065–R6068. https://doi.org/10.1103/PhysRevB.62.R6065.
54. Taguchi, Y.; Oohara, Y.; Yoshizawa, H.; Nagaosa, N.; Tokura, Y. Spin chirality, Berry phase, and anomalous Hall effect in a frustrated ferromagnet. *Science* **2001**, *291*, 2573–2576. https://doi.org/10.1126/science.1058161.
55. Tatara, G.; Kawamura, H. Chirality-driven anomalous Hall effect in weak coupling regime. *J. Phys. Soc. Jpn.* **2002**, *71*, 2613–2616. https://doi.org/10.1143/JPSJ.71.2613.
56. Hamamoto, K.; Ezawa, M.; Nagaosa, N. Quantized topological Hall effect in skyrmion crystal. *Phys. Rev. B* **2015**, *92*, 115417. https://doi.org/10.1103/PhysRevB.92.115417.
57. Everschor, K.; Garst, M.; Duine, R.A.; Rosch, A. Current-induced rotational torques in the skyrmion lattice phase of chiral magnets. *Phys. Rev. B* **2011**, *84*, 064401. https://doi.org/10.1103/PhysRevB.84.064401.
58. Everschor, K.; Garst, M.; Binz, B.; Jonietz, F.; Mühlbauer, S.; Pfleiderer, C.; Rosch, A. Rotating skyrmion lattices by spin torques and field or temperature gradients. *Phys. Rev. B* **2012**, *86*, 054432. https://doi.org/10.1103/PhysRevB.86.054432.
59. Mochizuki, M. Spin-Wave Modes and Their Intense Excitation Effects in Skyrmion Crystals. *Phys. Rev. Lett.* **2012**, *108*, 017601. https://doi.org/10.1103/PhysRevLett.108.017601.
60. Tatara, G.; Fukuyama, H. Phasons and excitations in skyrmion lattice. *J. Phys. Soc. Jpn.* **2014**, *83*, 104711. https://doi.org/https://doi.org/10.7566/JPSJ.83.104711.
61. Lin, S.Z.; Batista, C.D.; Saxena, A. Internal modes of a skyrmion in the ferromagnetic state of chiral magnets. *Phys. Rev. B* **2014**, *89*, 024415. https://doi.org/10.1103/PhysRevB.89.024415.
62. Garst, M.; Waizner, J.; Grundler, D. Collective spin excitations of helices and magnetic skyrmions: review and perspectives of magnonics in non-centrosymmetric magnets. *J. Phys. D* **2017**, *50*, 293002. https://doi.org/10.1088/1361-6463/aa7573.
63. Yi, S.D.; Onoda, S.; Nagaosa, N.; Han, J.H. Skyrmions and anomalous Hall effect in a Dzyaloshinskii-Moriya spiral magnet. *Phys. Rev. B* **2009**, *80*, 054416. https://doi.org/10.1103/PhysRevB.80.054416.

 doi:10.20944/preprints202602.0033.v1

64. Binz, B.; Vishwanath, A.; Aji, V. Theory of the Helical Spin Crystal: A Candidate for the Partially Ordered State of MnSi. *Phys. Rev. Lett.* **2006**, *96*, 207202. https://doi.org/10.1103/PhysRevLett.96.207202.
65. Binz, B.; Vishwanath, A. Theory of helical spin crystals: Phases, textures, and properties. *Phys. Rev. B* **2006**, *74*, 214408. https://doi.org/10.1103/PhysRevB.74.214408.
66. Hayami, S.; Okubo, T.; Motome, Y. Phase shift in skyrmion crystals. *Nat. Commun.* **2021**, *12*, 6927. https://doi.org/10.1038/s41467-021-27083-0.
67. Okubo, T.; Chung, S.; Kawamura, H. Multiple-q States and the Skyrmion Lattice of the Triangular-Lattice Heisenberg Antiferromagnet under Magnetic Fields. *Phys. Rev. Lett.* **2012**, *108*, 017206. https://doi.org/10.1103/PhysRevLett.108.017206.
68. Leonov, A.O.; Mostovoy, M. Multiply periodic states and isolated skyrmions in an anisotropic frustrated magnet. *Nat. Commun.* **2015**, *6*, 8275. https://doi.org/10.1038/ncomms9275.
69. Hayami, S.; Lin, S.Z.; Kamiya, Y.; Batista, C.D. Vortices, skyrmions, and chirality waves in frustrated Mott insulators with a quenched periodic array of impurities. *Phys. Rev. B* **2016**, *94*, 174420. https://doi.org/10.1103/PhysRevB.94.174420.
70. Hayami, S. In-plane magnetic field-induced skyrmion crystal in frustrated magnets with easy-plane anisotropy. *Phys. Rev. B* **2021**, *103*, 224418. https://doi.org/10.1103/PhysRevB.103.224418.
71. Kawamura, H. Frustration-induced skyrmion crystals in centrosymmetric magnets. *J. Phys.: Condens. Matter* **2025**, *37*, 183004. https://doi.org/10.1088/1361-648X/adbf5b.
72. Butenko, A.B.; Leonov, A.A.; Rößler, U.K.; Bogdanov, A.N. Stabilization of skyrmion textures by uniaxial distortions in noncentrosymmetric cubic helimagnets. *Phys. Rev. B* **2010**, *82*, 052403. https://doi.org/10.1103/PhysRevB.82.052403.
73. Wilson, M.N.; Butenko, A.B.; Bogdanov, A.N.; Monchesky, T.L. Chiral skyrmions in cubic helimagnet films: The role of uniaxial anisotropy. *Phys. Rev. B* **2014**, *89*, 094411. https://doi.org/10.1103/PhysRevB.89.094411.
74. Lin, S.Z.; Saxena, A.; Batista, C.D. Skyrmion fractionalization and merons in chiral magnets with easy-plane anisotropy. *Phys. Rev. B* **2015**, *91*, 224407. https://doi.org/10.1103/PhysRevB.91.224407.
75. Leonov, A.O.; Monchesky, T.L.; Romming, N.; Kubetzka, A.; Bogdanov, A.N.; Wiesendanger, R. The properties of isolated chiral skyrmions in thin magnetic films. *New. J. Phys.* **2016**, *18*, 065003. https://doi.org/10.1088/1367-2630/18/6/065003.
76. Ehlers, D.; Stasinopoulos, I.; Tsurkan, V.; Krug von Nidda, H.A.; Fehér, T.; Leonov, A.; Kézsmárki, I.; Grundler, D.; Loidl, A. Skyrmion dynamics under uniaxial anisotropy. *Phys. Rev. B* **2016**, *94*, 014406. https://doi.org/10.1103/PhysRevB.94.014406.
77. Leonov, A.O.; Kézsmárki, I. Skyrmion robustness in noncentrosymmetric magnets with axial symmetry: The role of anisotropy and tilted magnetic fields. *Phys. Rev. B* **2017**, *96*, 214413. https://doi.org/10.1103/PhysRevB.96.214413.
78. Gross, B.; Philipp, S.; Geirhos, K.; Mehlin, A.; Bordács, S.; Tsurkan, V.; Leonov, A.; Kézsmárki, I.; Poggio, M. Stability of Néel-type skyrmion lattice against oblique magnetic fields in GaV_4S_8 and GaV_4Se_8. *Phys. Rev. B* **2020**, *102*, 104407. https://doi.org/10.1103/PhysRevB.102.104407.
79. Hayami, S. Multiple-Q magnetism by anisotropic bilinear-biquadratic interactions in momentum space. *J. Magn. Magn. Mater.* **2020**, *513*, 167181. https://doi.org/10.1016/j.jmmm.2020.167181.
80. Utesov, O.I. Thermodynamically stable skyrmion lattice in a tetragonal frustrated antiferromagnet with dipolar interaction. *Phys. Rev. B* **2021**, *103*, 064414. https://doi.org/10.1103/PhysRevB.103.064414.
81. Utesov, O.I. Mean-field description of skyrmion lattice in hexagonal frustrated antiferromagnets. *Phys. Rev. B* **2022**, *105*, 054435. https://doi.org/10.1103/PhysRevB.105.054435.
82. Hayami, S. Skyrmion crystal and spiral phases in centrosymmetric bilayer magnets with staggered Dzyaloshinskii-Moriya interaction. *Phys. Rev. B* **2022**, *105*, 014408. https://doi.org/10.1103/PhysRevB.105.014408.
83. Lin, S.Z. Skyrmion lattice in centrosymmetric magnets with local Dzyaloshinsky-Moriya interaction. *Mater. Today Quantum* **2024**, *2*, 100006. https://doi.org/https://doi.org/10.1016/j.mtquan.2024.100006.
84. Tokunaga, Y.; Yu, X.; White, J.; Rønnow, H.M.; Morikawa, D.; Taguchi, Y.; Tokura, Y. A new class of chiral materials hosting magnetic skyrmions beyond room temperature. *Nat. Commun.* **2015**, *6*, 7638. https://doi.org/10.1038/ncomms8638.
85. Karube, K.; White, J.; Reynolds, N.; Gavilano, J.; Oike, H.; Kikkawa, A.; Kagawa, F.; Tokunaga, Y.; Rønnow, H.M.; Tokura, Y.; et al. Robust metastable skyrmions and their triangular–square lattice structural transition in a high-temperature chiral magnet. *Nat. Mater.* **2016**, *15*, 1237. https://doi.org/10.1038/nmat4752.

 doi:10.20944/preprints202602.0033.v1

86. Karube, K.; White, J.S.; Morikawa, D.; Dewhurst, C.D.; Cubitt, R.; Kikkawa, A.; Yu, X.; Tokunaga, Y.; Arima, T.h.; Rønnow, H.M.; et al. Disordered skyrmion phase stabilized by magnetic frustration in a chiral magnet. *Sci. Adv.* **2018**, *4*, eaar7043. https://doi.org/10.1126/sciadv.aar7043.
87. Karube, K.; White, J.S.; Ukleev, V.; Dewhurst, C.D.; Cubitt, R.; Kikkawa, A.; Tokunaga, Y.; Rønnow, H.M.; Tokura, Y.; Taguchi, Y. Metastable skyrmion lattices governed by magnetic disorder and anisotropy in β-Mn-type chiral magnets. *Phys. Rev. B* **2020**, *102*, 064408. https://doi.org/10.1103/PhysRevB.102.064408.
88. Henderson, M.E.; Bleuel, M.; Beare, J.; Cory, D.G.; Heacock, B.; Huber, M.G.; Luke, G.M.; Pula, M.; Sarenac, D.; Sharma, S.; et al. Skyrmion alignment and pinning effects in the disordered multiphase skyrmion material $Co_8Zn_8Mn_4$. *Phys. Rev. B* **2022**, *106*, 094435. https://doi.org/10.1103/PhysRevB.106.094435.
89. Chacon, A.; Heinen, L.; Halder, M.; Bauer, A.; Simeth, W.; Mühlbauer, S.; Berger, H.; Garst, M.; Rosch, A.; Pfleiderer, C. Observation of two independent skyrmion phases in a chiral magnetic material. *Nat. Phys.* **2018**, *14*, 936–941. https://doi.org/10.1038/s41567-018-0184-y.
90. Takagi, R.; Yamasaki, Y.; Yokouchi, T.; Ukleev, V.; Yokoyama, Y.; Nakao, H.; Arima, T.; Tokura, Y.; Seki, S. Particle-size dependent structural transformation of skyrmion lattice. *Nat. Commun.* **2020**, *11*, 5685. https://doi.org/10.1038/s41467-020-19480-8.
91. Khanh, N.D.; Nakajima, T.; Yu, X.; Gao, S.; Shibata, K.; Hirschberger, M.; Yamasaki, Y.; Sagayama, H.; Nakao, H.; Peng, L.; et al. Nanometric square skyrmion lattice in a centrosymmetric tetragonal magnet. *Nat. Nanotechnol.* **2020**, *15*, 444. https://doi.org/10.1038/s41565-020-0684-7.
92. Matsuyama, N.; Nomura, T.; Imajo, S.; Nomoto, T.; Arita, R.; Sudo, K.; Kimata, M.; Khanh, N.D.; Takagi, R.; Tokura, Y.; et al. Quantum oscillations in the centrosymmetric skyrmion-hosting magnet $GdRu_2Si_2$. *Phys. Rev. B* **2023**, *107*, 104421. https://doi.org/10.1103/PhysRevB.107.104421.
93. Wood, G.D.A.; Khalyavin, D.D.; Mayoh, D.A.; Bouaziz, J.; Hall, A.E.; Holt, S.J.R.; Orlandi, F.; Manuel, P.; Blügel, S.; Staunton, J.B.; et al. Double-Q ground state with topological charge stripes in the centrosymmetric skyrmion candidate $GdRu_2Si_2$. *Phys. Rev. B* **2023**, *107*, L180402. https://doi.org/10.1103/PhysRevB.107.L180402.
94. Eremeev, S.; Glazkova, D.; Poelchen, G.; Kraiker, A.; Ali, K.; Tarasov, A.V.; Schulz, S.; Kliemt, K.; Chulkov, E.V.; Stolyarov, V.; et al. Insight into the electronic structure of the centrosymmetric skyrmion magnet $GdRu_2Si_2$. *Nanoscale Adv.* **2023**, *5*, 6678–6687. https://doi.org/https://doi.org/10.1039/D3NA00435J.
95. Dong, Y.; Kinoshita, Y.; Ochi, M.; Nakachi, R.; Higashinaka, R.; Hayami, S.; Wan, Y.; Arai, Y.; Huh, S.; Hashimoto, M.; et al. Pseudogap and Fermi arc induced by Fermi surface nesting in a centrosymmetric skyrmion magnet. *Science* **2025**, *388*, 624–630. https://doi.org/10.1126/science.adj7710.
96. Singh, D.; Fujishiro, Y.; Hayami, S.; Moody, S.H.; Nomoto, T.; Baral, P.R.; Ukleev, V.; Cubitt, R.; Steinke, N.J.; Gawryluk, D.J.; et al. Transition between distinct hybrid skyrmion textures through their hexagonal-to-square crystal transformation in a polar magnet. *Nat. Commun.* **2023**, *14*, 8050. https://doi.org/https://doi.org/10.1038/s41467-023-43814-x.
97. Hayami, S. Multiple skyrmion crystal phases by itinerant frustration in centrosymmetric tetragonal magnets. *J. Phys. Soc. Jpn.* **2022**, *91*, 023705. https://doi.org/10.7566/JPSJ.91.023705.
98. Hayami, S. Rectangular and square skyrmion crystals on a centrosymmetric square lattice with easy-axis anisotropy. *Phys. Rev. B* **2022**, *105*, 174437. https://doi.org/10.1103/PhysRevB.105.174437.
99. Wang, Z.; Su, Y.; Lin, S.Z.; Batista, C.D. Meron, skyrmion, and vortex crystals in centrosymmetric tetragonal magnets. *Phys. Rev. B* **2021**, *103*, 104408. https://doi.org/10.1103/PhysRevB.103.104408.
100. Hayami, S.; Yambe, R. Helicity locking of a square skyrmion crystal in a centrosymmetric lattice system without vertical mirror symmetry. *Phys. Rev. B* **2022**, *105*, 104428. https://doi.org/10.1103/PhysRevB.105.104428.
101. Zha, Y.; Hayami, S. Square skyrmion lattice in multiorbital f-electron systems. *Phys. Rev. B* **2025**, *111*, 165155. https://doi.org/10.1103/PhysRevB.111.165155.
102. Hayami, S.; Yambe, R. Stabilization mechanisms of magnetic skyrmion crystal and multiple-Q states based on momentum-resolved spin interactions. *Mater. Today Quantum* **2024**, *3*, 100010. https://doi.org/https://doi.org/10.1016/j.mtquan.2024.100010.
103. Bogdanov, A.N.; Rößler, U.K. Chiral Symmetry Breaking in Magnetic Thin Films and Multilayers. *Phys. Rev. Lett.* **2001**, *87*, 037203. https://doi.org/10.1103/PhysRevLett.87.037203.
104. Shibata, K.; Iwasaki, J.; Kanazawa, N.; Aizawa, S.; Tanigaki, T.; Shirai, M.; Nakajima, T.; Kubota, M.; Kawasaki, M.; Park, H.; et al. Large anisotropic deformation of skyrmions in strained crystal. *Nat. Nanotechnol.* **2015**, *10*, 589–592. https://doi.org/10.1038/nnano.2015.113.

 doi:10.20944/preprints202602.0033.v1

105. Wang, J.; Shi, Y.; Kamlah, M. Uniaxial strain modulation of the skyrmion phase transition in ferromagnetic thin films. *Phys. Rev. B* **2018**, *97*, 024429. https://doi.org/10.1103/PhysRevB.97.024429.
106. Osorio, S.A.; Sturla, M.B.; Rosales, H.D.; Cabra, D.C. From skyrmions to $\mathbb{Z}_2$ vortices in distorted chiral antiferromagnets. *Phys. Rev. B* **2019**, *100*, 220404. https://doi.org/10.1103/PhysRevB.100.220404.
107. El Hog, S.; Kato, F.; Koibuchi, H.; Diep, H.T. Finsler geometry modeling and Monte Carlo study of skyrmion shape deformation by uniaxial stress. *Phys. Rev. B* **2021**, *104*, 024402. https://doi.org/10.1103/PhysRevB.104.024402.
108. Hayami, S. Orthorhombic distortion and rectangular skyrmion crystal in a centrosymmetric tetragonal host. *J. Phys.: Mater.* **2023**, *6*, 014006. https://doi.org/10.1088/2515-7639/acab89.
109. Shang, T.; Xu, Y.; Gawryluk, D.J.; Ma, J.Z.; Shiroka, T.; Shi, M.; Pomjakushina, E. Anomalous Hall resistivity and possible topological Hall effect in the $EuAl_4$ antiferromagnet. *Phys. Rev. B* **2021**, *103*, L020405. https://doi.org/10.1103/PhysRevB.103.L020405.
110. Shimomura, S.; Murao, H.; Tsutsui, S.; Nakao, H.; Nakamura, A.; Hedo, M.; Nakama, T.; Ōnuki, Y. Lattice modulation and structural phase transition in the antiferromagnet EuAl4. *J. Phys. Soc. Jpn.* **2019**, *88*, 014602.
111. Kaneko, K.; Kawasaki, T.; Nakamura, A.; Munakata, K.; Nakao, A.; Hanashima, T.; Kiyanagi, R.; Ohhara, T.; Hedo, M.; Nakama, T.; et al. Charge-Density-Wave Order and Multiple Magnetic Transitions in Divalent Europium Compound $EuAl_4$. *J. Phys. Soc. Jpn.* **2021**, *90*, 064704. https://doi.org/10.7566/JPSJ.90.064704.
112. Takagi, R.; Matsuyama, N.; Ukleev, V.; Yu, L.; White, J.S.; Francoual, S.; Mardegan, J.R.L.; Hayami, S.; Saito, H.; Kaneko, K.; et al. Square and rhombic lattices of magnetic skyrmions in a centrosymmetric binary compound. *Nat. Commun.* **2022**, *13*, 1472. https://doi.org/10.1038/s41467-022-29131-9.
113. Gen, M.; Takagi, R.; Watanabe, Y.; Kitou, S.; Sagayama, H.; Matsuyama, N.; Kohama, Y.; Ikeda, A.; Ōnuki, Y.; Kurumaji, T.; et al. Rhombic skyrmion lattice coupled with orthorhombic structural distortion in $EuAl_4$. *Phys. Rev. B* **2023**, *107*, L020410. https://doi.org/10.1103/PhysRevB.107.L020410.
114. Nakatsuji, S.; Nambu, Y.; Tonomura, H.; Sakai, O.; Jonas, S.; Broholm, C.; Tsunetsugu, H.; Qiu, Y.; Maeno, Y. Spin disorder on a triangular lattice. *Science* **2005**, *309*, 1697–1700. https://doi.org/10.1126/science.1114727.
115. Day, P.; Moore, M.W.; Wilkinson, C.; Ziebeck, K.R.A. Neutron diffraction study of the incommensurate magnetic phase of $Ni_{0.92}Zn_{0.08}Br_2$. *J. Phys. C: Solid State Physics* **1981**, *14*, 3423. https://doi.org/10.1088/0022-3719/14/23/018.
116. Regnault, L.; Rossat-Mignod, J.; Adam, A.; Billerey, D.; Terrier, C. Inelastic neutron scattering investigation of the magnetic excitations in the helimagnetic state of $NiBr_2$. *Journal de Physique* **1982**, *43*, 1283–1290. https://doi.org/10.1051/jphys:019820043080128300.
117. Ghimire, N.; Ronning, F.; Williams, D.; Scott, B.; Luo, Y.; Thompson, J.; Bauer, E. Investigation of the physical properties of the tetragonal $CeMAl_4Si_2$ (M = Rh, Ir, Pt) compounds. *J. Phys.: Condens. Matter* **2014**, *27*, 025601. https://doi.org/10.1088/0953-8984/27/2/025601.
118. Gunasekera, J.; Harriger, L.; Dahal, A.; Maurya, A.; Heitmann, T.; Disseler, S.M.; Thamizhavel, A.; Dhar, S.; Singh, D.J.; Singh, D.K. Electronic nature of the lock-in magnetic transition in $CeXAl_4Si_2$. *Phys. Rev. B* **2016**, *93*, 155151. https://doi.org/10.1103/PhysRevB.93.155151.
119. Ruderman, M.A.; Kittel, C. Indirect Exchange Coupling of Nuclear Magnetic Moments by Conduction Electrons. *Phys. Rev.* **1954**, *96*, 99–102. https://doi.org/10.1103/PhysRev.96.99.
120. Kasuya, T. A Theory of Metallic Ferro- and Antiferromagnetism on Zener's Model. *Prog. Theor. Phys.* **1956**, *16*, 45–57. https://doi.org/10.1143/PTP.16.45.
121. Yosida, K. Magnetic Properties of Cu-Mn Alloys. *Phys. Rev.* **1957**, *106*, 893–898. https://doi.org/10.1103/PhysRev.106.893.
122. Yoshimori, A. A new type of antiferromagnetic structure in the rutile type crystal. *J. Phys. Soc. Jpn.* **1959**, *14*, 807–821.
123. Kaplan, T.A. Some Effects of Anisotropy on Spiral Spin-Configurations with Application to Rare-Earth Metals. *Phys. Rev.* **1961**, *124*, 329–339. https://doi.org/10.1103/PhysRev.124.329.
124. Elliott, R.J. Phenomenological Discussion of Magnetic Ordering in the Heavy Rare-Earth Metals. *Phys. Rev.* **1961**, *124*, 346–353. https://doi.org/10.1103/PhysRev.124.346.
125. Takagi, R.; White, J.; Hayami, S.; Arita, R.; Honecker, D.; Rønnow, H.; Tokura, Y.; Seki, S. Multiple-q noncollinear magnetism in an itinerant hexagonal magnet. *Sci. Adv.* **2018**, *4*, eaau3402. https://doi.org/10.1126/sciadv.aau3402.
126. Hayami, S.; Yambe, R. Field-Direction Sensitive Skyrmion Crystals in Cubic Chiral Systems: Implication to $4f$-Electron Compound EuPtSi. *J. Phys. Soc. Jpn.* **2021**, *90*, 073705. https://doi.org/10.7566/JPSJ.90.073705.

 doi:10.20944/preprints202602.0033.v1

127. Becker, M.; Hermanns, M.; Bauer, B.; Garst, M.; Trebst, S. Spin-orbit physics of $j = \frac{1}{2}$ Mott insulators on the triangular lattice. *Phys. Rev. B* **2015**, *91*, 155135. https://doi.org/10.1103/PhysRevB.91.155135.
128. Hayami, S.; Yambe, R. Degeneracy Lifting of Néel, Bloch, and Anti-Skyrmion Crystals in Centrosymmetric Tetragonal Systems. *J. Phys. Soc. Jpn.* **2020**, *89*, 103702. https://doi.org/10.7566/JPSJ.89.103702.
129. Amoroso, D.; Barone, P.; Picozzi, S. Spontaneous skyrmionic lattice from anisotropic symmetric exchange in a Ni-halide monolayer. *Nat. Commun.* **2020**, *11*, 5784. https://doi.org/10.1038/s41467-020-19535-w.
130. Hayami, S.; Motome, Y. Noncoplanar multiple-Q spin textures by itinerant frustration: Effects of single-ion anisotropy and bond-dependent anisotropy. *Phys. Rev. B* **2021**, *103*, 054422. https://doi.org/10.1103/PhysRevB.103.054422.
131. Yambe, R.; Hayami, S. Skyrmion crystals in centrosymmetric itinerant magnets without horizontal mirror plane. *Sci. Rep.* **2021**, *11*, 11184. https://doi.org/10.1038/s41598-021-90308-1.
132. Amoroso, D.; Barone, P.; Picozzi, S. Interplay between Single-Ion and Two-Ion Anisotropies in Frustrated 2D Semiconductors and Tuning of Magnetic Structures Topology. *Nanomaterials* **2021**, *11*, 1873. https://doi.org/10.3390/nano11081873.
133. Hayami, S.; Kato, Y. Widely-sweeping magnetic field–temperature phase diagrams for skyrmion-hosting centrosymmetric tetragonal magnets. *J. Magn. Magn. Mater.* **2023**, *571*, 170547. https://doi.org/https://doi.org/10.1016/j.jmmm.2023.170547.
134. Yambe, R.; Hayami, S. Effective spin model in momentum space: Toward a systematic understanding of multiple-Q instability by momentum-resolved anisotropic exchange interactions. *Phys. Rev. B* **2022**, *106*, 174437. https://doi.org/10.1103/PhysRevB.106.174437.